Research Article | Vol. 25, No. 7 | 3 Apr 2017 | OPTICS EXPRESS 7761
Optics EXPRESS

High speed, wide velocity dynamic range Doppler optical coherence tomography (Part V): Optimal utilization of multi-beam scanning for Doppler and speckle variance microvascular imaging

CHAOLIANG CHEN,[1,2,4] KYLE H. Y. CHENG,[2] RAPHAEL JAKUBOVIC,[3] JAMIL JIVRAJ,[2] JOEL RAMJIST,[2] RYAN DEORAJH,[2] WANRONG GAO,[1] ELIZABETH BARNES,[4] LEE CHIN,[5] AND VICTOR X. D. YANG[2,3,6,7,*]

[1]*Department of Optical Engineering, Nanjing University of Science and Technology, Nanjing, Jiangsu, China*
[2]*Biophotonics and Bioengineering Lab, Department of Electrical and Computer Engineering, Ryerson University, Toronto, Ontario, Canada*
[3]*Department of Biomedical Physics, Ryerson University, Toronto, Ontario, Canada*
[4]*Department of Radiation Oncology, Odette Cancer Centre, Sunnybrook Health Sciences Centre, Toronto, Ontario, Canada*
[5]*Department of Medical Physics, Odette Cancer Centre, Sunnybrook Health Sciences Centre, Toronto, Ontario, Canada*
[6]*Division of Neurosurgery, Sunnybrook Health Sciences Centre, Toronto, Ontario, Canada*
[7]*Division of Neurosurgery, Faculty of Medicine, University of Toronto, Toronto, Ontario, Canada*
[*]*yangv@ryerson.ca*

Abstract: In this paper, a multi-beam scanning technique is proposed to optimize the microvascular images of human skin obtained with Doppler effect based methods and speckle variance processing. Flow phantom experiments were performed to investigate the suitability for combining multi-beam data to achieve enhanced microvascular imaging. To our surprise, the highly variable spot sizes (ranging from 13 to 77 μm) encountered in high numerical aperture multi-beam OCT system imaging the same target provided reasonably uniform Doppler variance and speckle variance responses as functions of flow velocity, which formed the basis for combining them to obtain better microvascular imaging without scanning penalty. *In vivo* 2D and 3D imaging of human skin was then performed to further demonstrate the benefit of combining multi-beam scanning to obtain improved signal-to-noise ratio (SNR) in microvascular imaging. Such SNR improvement can be as high as 10 dB. To our knowledge, this is the first demonstration of combining different spot size, staggered multiple optical foci scanning, to achieve enhanced SNR for blood flow OCT imaging.

OCIS codes: (110.4500) Optical coherence tomography; (170.3880) Medical and biological imaging; (100.6950) Tomographic image processing.

References and links

1. D. Huang, E. A. Swanson, C. P. Lin, J. S. Schuman, W. G. Stinson, W. Chang, M. R. Hee, T. Flotte, K. Gregory, C. A. Puliafito, and J. G. Fujimoto, "Optical coherence tomography," Science **254**(5035), 1178–1181 (1991).
2. Z. Chen, T. E. Milner, D. Dave, and J. S. Nelson, "Optical Doppler tomographic imaging of fluid flow velocity in highly scattering media," Opt. Lett. **22**(1), 64–66 (1997).
3. Z. Chen, T. E. Milner, S. Srinivas, X. Wang, A. Malekafzali, M. J. C. van Gemert, and J. S. Nelson, "Noninvasive imaging of *in vivo* blood flow velocity using optical Doppler tomography," Opt. Lett. **22**(14), 1119–1121 (1997).
4. D. P. Davé and T. E. Milner, "Doppler-angle measurement in highly scattering media," Opt. Lett. **25**(20), 1523–1525 (2000).

#285089 https://doi.org/10.1364/OE.25.007761
Journal © 2017 Received 18 Jan 2017; revised 13 Mar 2017; accepted 16 Mar 2017; published 27 Mar 2017

Optics EXPRESS

5. R. M. Werkmeister, N. Dragostinoff, M. Pircher, E. Götzinger, C. K. Hitzenberger, R. A. Leitgeb, and L. Schmetterer, "Bidirectional Doppler Fourier-domain optical coherence tomography for measurement of absolute flow velocities in human retinal vessels," Opt. Lett. **33**(24), 2967–2969 (2008).
6. C. Blatter, S. Coquoz, B. Grajciar, A. S. G. Singh, M. Bonesi, R. M. Werkmeister, L. Schmetterer, and R. A. Leitgeb, "Dove prism based rotating dual beam bidirectional Doppler OCT," Biomed. Opt. Express **4**(7), 1188–1203 (2013).
7. Y. Wang, B. A. Bower, J. A. Izatt, O. Tan, and D. Huang, "*In vivo* total retinal blood flow measurement by Fourier domain Doppler optical coherence tomography," J. Biomed. Opt. **12**(4), 041215 (2007).
8. V. Yang, M. Gordon, B. Qi, J. Pekar, S. Lo, E. Seng-Yue, A. Mok, B. Wilson, and I. Vitkin, "High speed, wide velocity dynamic range Doppler optical coherence tomography (Part I): System design, signal processing, and performance," Opt. Express **11**(7), 794–809 (2003).
9. C. Dai, X. Liu, H. F. Zhang, C. A. Puliafito, and S. Jiao, "Absolute retinal Blood Flow Measurement With a Dual-Beam Doppler Optical Coherence Tomography," Invest. Ophthalmol. Vis. Sci. **54**(13), 7998–8003 (2013).
10. R. Haindl, W. Trasischker, A. Wartak, B. Baumann, M. Pircher, and C. K. Hitzenberger, "Total retinal blood flow measurement by three beam Doppler optical coherence tomography," Biomed. Opt. Express **7**(2), 287–301 (2016).
11. Y. Zhao, Z. Chen, C. Saxer, Q. Shen, S. Xiang, J. F. de Boer, and J. S. Nelson, "Doppler standard deviation imaging for clinical monitoring of *in vivo* human skin blood flow," Opt. Lett. **25**(18), 1358–1360 (2000).
12. H. Ren, K. M. Brecke, Z. Ding, Y. Zhao, J. S. Nelson, and Z. Chen, "Imaging and quantifying transverse flow velocity with the Doppler bandwidth in a phase-resolved functional optical coherence tomography," Opt. Lett. **27**(6), 409–411 (2002).
13. H. Ren, Z. Ding, Y. Zhao, J. Miao, J. S. Nelson, and Z. Chen, "Phase-resolved functional optical coherence tomography: simultaneous imaging of in situ tissue structure, blood flow velocity, standard deviation, birefringence, and Stokes vectors in human skin," Opt. Lett. **27**(19), 1702–1704 (2002).
14. G. Liu, L. Chou, W. Jia, W. Qi, B. Choi, and Z. Chen, "Intensity-based modified Doppler variance algorithm: application to phase instable and phase stable optical coherence tomography systems," Opt. Express **19**(12), 11429–11440 (2011).
15. J. Barton and S. Stromski, "Flow measurement without phase information in optical coherence tomography images," Opt. Express **13**(14), 5234–5239 (2005).
16. A. Mariampillai, B. A. Standish, E. H. Moriyama, M. Khurana, N. R. Munce, M. K. Leung, J. Jiang, A. Cable, B. C. Wilson, I. A. Vitkin, and V. X. Yang, "Speckle variance detection of microvasculature using swept-source optical coherence tomography," Opt. Lett. **33**(13), 1530–1532 (2008).
17. A. Mariampillai, M. K. K. Leung, M. Jarvi, B. A. Standish, K. Lee, B. C. Wilson, A. Vitkin, and V. X. D. Yang, "Optimized speckle variance OCT imaging of microvasculature," Opt. Lett. **35**(8), 1257–1259 (2010).
18. D. W. Cadotte, A. Mariampillai, A. Cadotte, K. K. Lee, T.-R. Kiehl, B. C. Wilson, M. G. Fehlings, and V. X. Yang, "Speckle variance optical coherence tomography of the rodent spinal cord: *in vivo* feasibility," Biomed. Opt. Express **3**(5), 911–919 (2012).
19. J. Fingler, D. Schwartz, C. Yang, and S. E. Fraser, "Mobility and transverse flow visualization using phase variance contrast with spectral domain optical coherence tomography," Opt. Express **15**(20), 12636–12653 (2007).
20. J. Fingler, R. J. Zawadzki, J. S. Werner, D. Schwartz, and S. E. Fraser, "Volumetric microvascular imaging of human retina using optical coherence tomography with a novel motion contrast technique," Opt. Express **17**(24), 22190–22200 (2009).
21. D. Y. Kim, J. Fingler, J. S. Werner, D. M. Schwartz, S. E. Fraser, and R. J. Zawadzki, "*In vivo* volumetric imaging of human retinal circulation with phase-variance optical coherence tomography," Biomed. Opt. Express **2**(6), 1504–1513 (2011).
22. R. K. Wang, "Three-dimensional optical micro-angiography maps directional blood perfusion deep within microcirculation tissue beds *in vivo*," Phys. Med. Biol. **52**(23), N531–N537 (2007).
23. L. An, J. Qin, and R. K. Wang, "Ultrahigh sensitive optical microangiography for *in vivo* imaging of microcirculations within human skin tissue beds," Opt. Express **18**(8), 8220–8228 (2010).
24. L. An and R. K. Wang, "Full range complex ultrahigh sensitive optical microangiography," Opt. Lett. **36**(6), 831–833 (2011).
25. E. Jonathan, J. Enfield, and M. J. Leahy, "Correlation mapping method for generating microcirculation morphology from optical coherence tomography (OCT) intensity images," J. Biophotonics **4**(9), 583–587 (2011).
26. J. Enfield, E. Jonathan, and M. Leahy, "*In vivo* imaging of the microcirculation of the volar forearm using correlation mapping optical coherence tomography (cmOCT)," Biomed. Opt. Express **2**(5), 1184–1193 (2011).
27. H. M. Subhash and M. J. Leahy, "Microcirculation imaging based on full-range high-speed spectral domain correlation mapping optical coherence tomography," J. Biomed. Opt. **19**(2), 021103 (2014).
28. A. Doronin and I. Meglinski, "Imaging of subcutaneous microcirculation vascular network by double correlation optical coherence tomography," Laser Photonics Rev. **7**(5), 797–800 (2013).
29. P. Li, Y. Cheng, L. Zhou, C. Pan, Z. Ding, and P. Li, "Single-shot angular compounded optical coherence tomography angiography by splitting full-space B-scan modulation spectrum for flow contrast enhancement," Opt. Lett. **41**(5), 1058–1061 (2016).

30. P. Li, Y. Cheng, P. Li, L. Zhou, Z. Ding, Y. Ni, and C. Pan, "Hybrid averaging offers high-flow contrast by cost apportionment among imaging time, axial, and lateral resolution in optical coherence tomography angiography," Opt. Lett. **41**(17), 3944–3947 (2016).
31. Y. Cheng, L. Guo, C. Pan, T. Lu, T. Hong, Z. Ding, and P. Li, "Statistical analysis of motion contrast in optical coherence tomography angiography," J. Biomed. Opt. **20**(11), 116004 (2015).
32. V. X. Yang, N. Munce, J. Pekar, M. L. Gordon, S. Lo, N. E. Marcon, B. C. Wilson, and I. A. Vitkin, "Micromachined array tip for multifocus fiber-based optical coherence tomography," Opt. Lett. **29**(15), 1754–1756 (2004).
33. J. Holmes, S. Hattersley, N. Stone, F. Bazant-Hegemark, and H. Barr, "Multi-channel Fourier domain OCT system with superior lateral resolution for biomedical applications," Proc. SPIE **6847**, 68470O (2008).
34. M. Ulrich, T. von Braunmuehl, H. Kurzen, T. Dirschka, C. Kellner, E. Sattler, C. Berking, J. Welzel, and U. Reinhold, "The sensitivity and specificity of optical coherence tomography for the assisted diagnosis of nonpigmented basal cell carcinoma: an observational study," Br. J. Dermatol. **173**(2), 428–435 (2015).
35. J. M. Schmitt, S. H. Xiang, and K. M. Yung, "Speckle in optical coherence tomography," J. Biomed. Opt. **4**(1), 95–105 (1999).
36. B. Vakoc, S. Yun, J. de Boer, G. Tearney, and B. Bouma, "Phase-resolved optical frequency domain imaging," Opt. Express **13**(14), 5483–5493 (2005).
37. B. Park, M. C. Pierce, B. Cense, S. H. Yun, M. Mujat, G. Tearney, B. Bouma, and J. de Boer, "Real-time fiber-based multi-functional spectral-domain optical coherence tomography at 1.3 microm," Opt. Express **13**(11), 3931–3944 (2005).

1. Introduction

Optical coherence tomography (OCT) [1] as an emerging medical imaging modality is well suited for non-invasive *in vivo* applications with high imaging speed and near histological resolution. After ~25 years of development, a variety of extended functional OCT modalities have been investigated, such as color Doppler OCT (CDOCT) or phase sensitive OCT [2–10], Doppler variance OCT (DVOCT) or Doppler bandwidth OCT [11–14], speckle variance OCT (SVOCT) [15–18], phase variance OCT (PVOCT) [19–21], optical micro-angiography (OMAG) [22–24] and correlation mapping OCT (cmOCT) [25–28]. Recently, an angular compounded algorithm is also proposed by Li *et al.* for flow contrast enhancement [29–31]. These methods are widely used to extract blood flow signals in a variety of tissues. Utilization of multiple optical beams in blood flow imaging had been previously demonstrated, however, these are typically used for extraction of absolute velocity of blood flow especially in the case of accurate assessment of Doppler angle [9, 10] where 2 or 3 optical beams with a mutual focus were used.

Multi-channel or multi-beam OCT techniques [32, 33] were proposed previously to resolve conflicting requirements of high numerical aperture and optimal light source power utilization. In these setups, the multiple optical beams did not have a mutual focal point, and each beam had an optimal structural OCT imaging range near its focal zone with tight beam waist and four or more beams' data were stitched together to provide the final structural OCT image. When the focal points were staggered in the depth direction, any blood vessel within the imaging volume would be scanned across by multiple beams regardless of whether it was within the optimal focal zone. This effect provided an interesting opportunity where such multiple measurements of blood flow by the different optical beams can be exploited. A key question for such an approach remained as whether optical beams of different diameters were scanned across the same blood vessel would cause deleterious effects for blood flow imaging under *in vivo* conditions.

In this paper, we experimentally investigate the dependence of Doppler and speckle variance OCT imaging with different beam spot sizes occurring along the optical axis away from the focal spot. After establishing the relative independence to spot size changes, we demonstrate the potential of utilizing the multiple optical beams to provide better microvascular imaging of normal human skin and non-melanoma skin cancer *in vivo*.

2. Principle of multi-beam OCT scanning and relationship to wavefront

While multiple techniques [32, 33] exist, the principle of multi-beam OCT for improved spatial resolution relies on using high numerical aperture optical beams with digital stitching,

Optics EXPRESS

as illustrated in Fig. 1(a). We propose each of the OCT A-scan obtained from individual optical beams, including areas outside of its focal zone, can provide relevant blood flow information via image processing, such as averaging, to improve image signal to noise ratio (SNR), as illustrated in Fig. 1(b). A typical commercial multi-beam swept source optical coherence tomography (SSOCT) system (VivoSight, Michelson Diagnostics, Kent, UK) can produce focal spot ranging from 7.5 [34] to 10 μm [33]. Arbitrarily inserting a beam profiler, without deliberately matching the region of imaging to the focal spot of any one of the optical beams, which would be the common scenario of clinically imaging blood vessels, would yield of spot sizes as large as 77 μm. Figures 1(c)-1(e) show a typical set of beam profiler results, where the four optical beams showed different beam width across the imaging plane of the beam profiler.

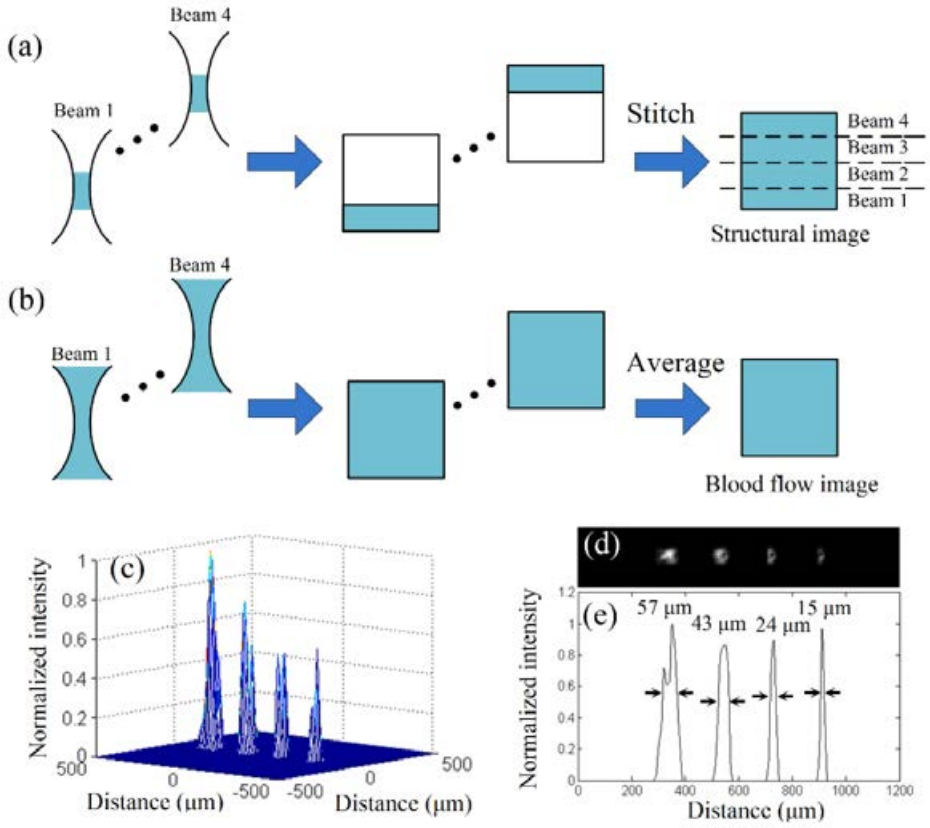

Fig. 1. (a) Multi-beam OCT structural image generation and stitching of individual foci. (b) Proposed multi-beam OCT blood flow imaging via averaging of data including regions outside of Rayleigh range. A typical beam profiler measurement of the four beams at an arbitrary depth (355 μm away from zero optical path length delay point relative to beam 1) showed different intensity (c), spot sizes (d) and (e).

Given the wide ranges of spot sizes encountered across the same imaging depth, one may inquire the pros and cons of averaging data for blood flow imaging. While spatial resolution is important for visualization of microvasculature, in many clinical scenarios, the ability to detect microvascular blood flow and vessel network is also important. We recognize that CDOCT, DVOCT and SVOCT all depend on wavefront interference, where the same wavefront propagates through the sample arm along the depth of tissue being imaged. The interference fringes of backscattered light from tissue and reference arm provided the sample

Optics EXPRESS

information at different depths. Figure 2 illustrates the wavefront propagation through a focal point in tissue, as adapted from Schmitt *et al.* [35].

Two main processes influence the spatial coherence of the returning wavefront: 1) multiple backscattering of the beam inside and outside of the desired sample volume; 2) random delays of the forward-propagating and returning beam caused by multiple forward scattering. The common feature of both processes is that they alter the shape of the wavefront of the returning beam and create localized regions of constructive and destructive interference that appear as speckle in OCT images.

Assuming a multi-beam system is constructed with sufficient similarity between the beams, one might conclude that wavefront distortions caused by target of interest, e.g., a blood vessel, which may or may not be at the focal spot of a particular beam, can be either forward or backward propagated through different depths along the beam, through the focal spot. In order words, the changes in speckle pattern or Doppler variance obtained by any particular beam would be equivalent to other optical beams within the multi-beam system.

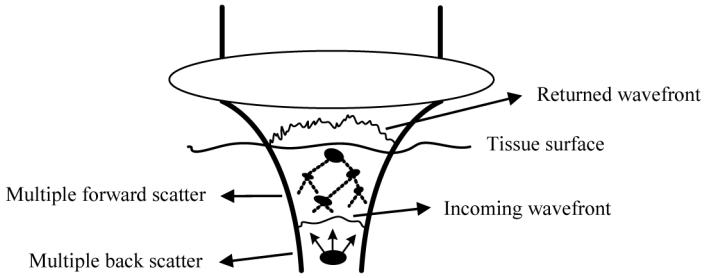

Fig. 2. Propagation of a focused optical beam in tissue with multiple scattering events and wavefront distortion. Adapted from Schmitt *et al.* [35].

In this paper, we set out to experimentally verify the above hypothesis. We would use flow phantoms to measure the Doppler variance and speckle variance OCT, to determine whether any dependence to spot size exist. We applied phase correction techniques to minimize measured phase error, such that detailed analysis of Doppler variance can be performed. We would determine the dependency of Doppler variance and speckle variance to flow velocity, and compare the four beams at multiple imaging depths. *In vivo* human volunteers as well as patient with non-pigmented skin cancer were also imaged, where 2D and 3D reconstructions of blood flow imaging were generated using information from all four optical beams.

3. Imaging experiments

3.1 OCT imaging system

All the experiments in this work were performed with a commercial SSOCT system (VivoSight, Michelson Diagnostics, Kent, UK). The light source (Axsun Technologies, USA) has a center wavelength of 1305 μm and operates at a scanning rate of 20 kHz. The best axial and lateral resolutions of this system are 10 μm and 7.5 μm, respectively. As shown in Fig. 3(a), the probe beam is divided into four beams, collimated and passed through x-y galvo scanners, finally refocused at different depths into the tissue of interest. The optical power of each beam is different, where the higher power beams are focused into deeper tissue, as a more efficient utilization of source power [32]. An example structural OCT image formation process is shown from Figs. 3(b)-3(e), where individual optical beams produced individual images of the entire target tissue, and a final image incorporating advanced stitching function is shown in Fig. 3(f). During *in vivo* imaging, 1100 A-scans over 2 mm were acquired in each B-scan for color Doppler and Doppler variance imaging. For SVOCT, each position was scanned twice and 240 × 1100 A-scans were obtained.

Optics EXPRESS

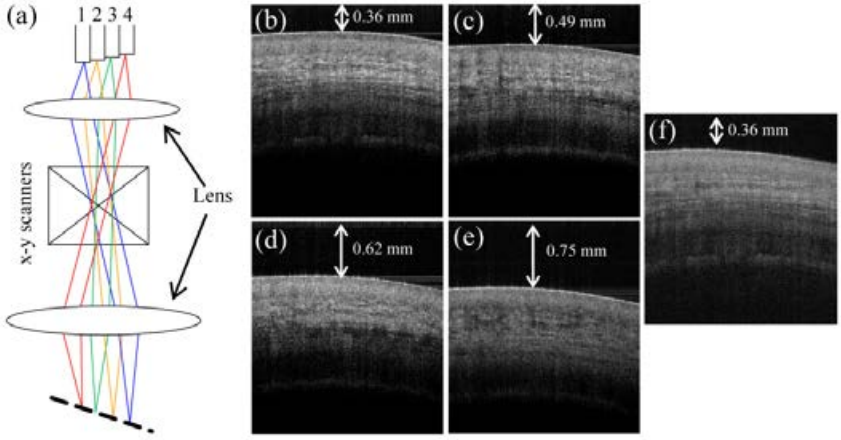

Fig. 3. (a) Schematics for four optical beams in the sample arm through collimating, focusing, and scanning optics. (b) - (e) are the individual structural images of human skin obtained with beam 1 - 4, respectively, with different offsets from zero optical path length delay point. (f) shows the stitched structural image.

3.2 Flow Phantom experiments

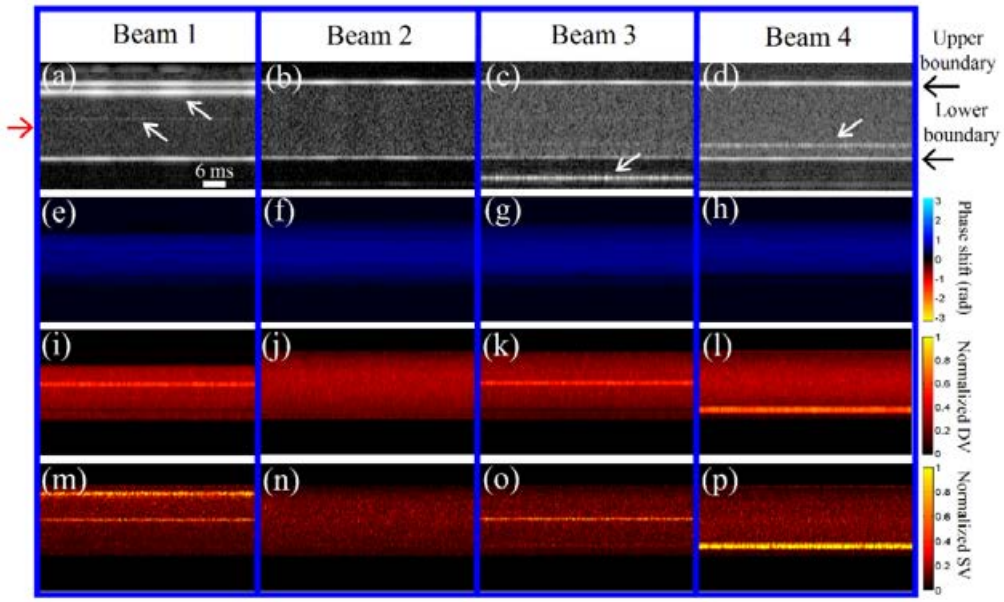

Fig. 4. Multi-beam OCT imaging of a rectangular channel phantom, where the flow channel (500 μm × 160 μm) was built with four cover slips. (a) - (d) are the structural images of the sample obtained by the four beams. (e) - (h) are the phase shift images obtained by the four beams with window size of 1 × 128 pixels. (i) - (l) are the Doppler variance images obtained by the four beams with window size of 1 × 8 pixels. (m) - (p) are the interline speckle variance images obtained by the four beams with window size of 1 × 2 pixels.

To study the influence of different beam spot size on Doppler variance and speckle variance, a flow phantom experiment was designed using a rectangular channel (500 μm × 160 μm) built with four cover slips. Intralipid solution at 0.5% was pumped by a syringe pump (Harvard Apparatus, Holliston, MA), achieving mean flow velocity up to 34 cm/s. M-mode imaging was performed using the above multi-beam OCT system, yielding 4 individual data sets of the same flow phantom, even though the optical path length for each beam was

Optics EXPRESS

different. Additional differences include different spot sizes of each beam were used to image the same location of the flow phantom, and each beam had slightly different Doppler angles. To avoid significant aliasing, the main optical axis of the multi-beam OCT system was aligned to nearly 90° from the direction of the flow. Figure 4 shows OCT images obtained by the four beams at mean flow velocity of 10.2 cm/s. Note the images had been cropped such that the flow phantom appears at the same depth, even though the optical path lengths were different. Figures 4(a)-4(d) are the structural images, where the transverse lines marked by white arrows are multiple reflections caused by the upper cover slip to air interface. Figures 4(e)-4(h) are phase shift images obtained by Kasai correlation technique [8] with 128 adjacent A-scans. The timing induced phase errors were removed using the lower boundary of the flow channel as a calibration signal as per Vakoc *et al*. [36]. Differences in the Doppler angle between the optical beams contribute to the slight differences in calculated phase shift.

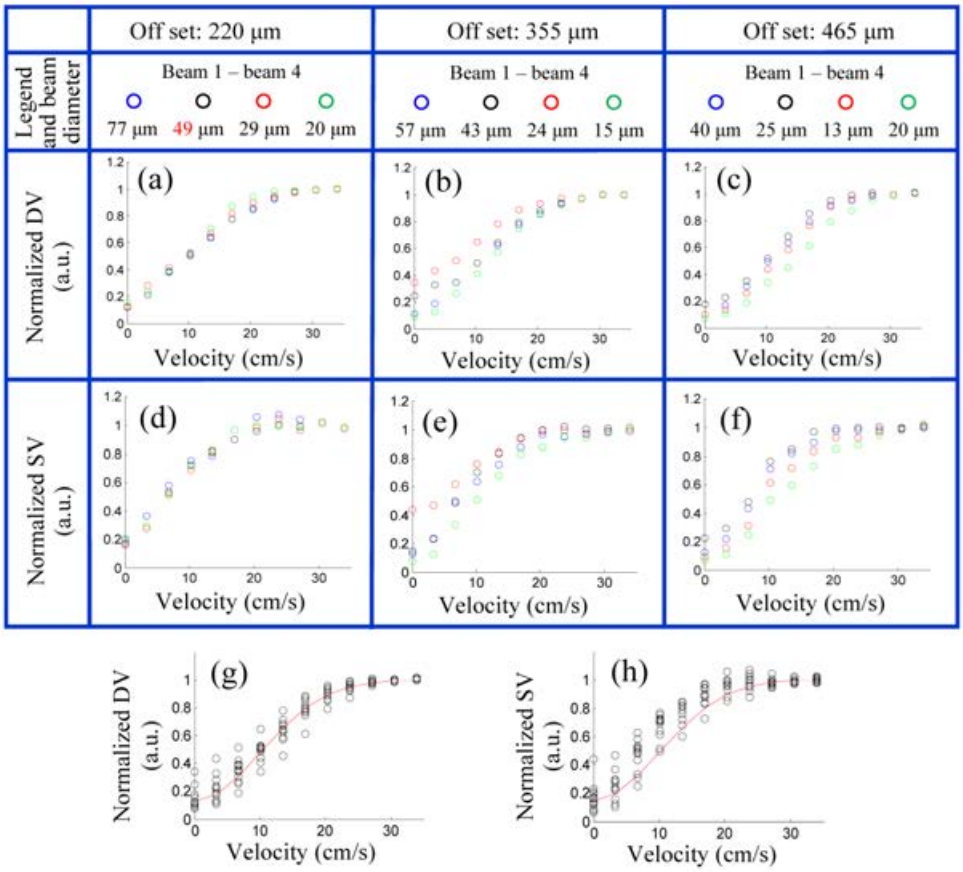

Fig. 5. Doppler variance and speckle variance at the depth position marked by red arrow in Fig. 4(a). Micrometer adjusted off set at 220, 355, and 465 μm allowed 12 different combinations of beam spot diameters across the 4 optical beams. Normalized Doppler variance (a) - (c) and normalized speckle variance (d) - (e) are plotted, respectively. Collapsing these plots together, we obtained the normalized PV (g) and SV (h) of multi-beam OCT as function of velocity of the flow phantom. The measured standard deviations of normalized PV and SV are in the range of 0.09, in agreement with theoretical [37] model (red lines) calculated with the lateral resolution at focus.

Doppler variance and speckle variance, on the other hand, were less dependent on Doppler angle as demonstrated previously [13, 16]. Therefore, Figs. 4(i)-4(l) are Doppler variance processed using 8 adjacent A-scans and Figs. 4(m)-4(p) are speckle variance

Optics EXPRESS

processed using 2 adjacent A-scans, for mean flow velocity of 10.2 cm/s. These are images of the phantom at the same flow rate, obtained by different optical beams 1 to 4, respectively. Given the similarity between the results obtained from each beam, the mean flow velocity was varied from 0 to 34 cm/s, and the peak values of speckle variance and Doppler variance from each beam were measured at the centre of the flow phantom channel (marked by red arrow in Fig. 4(a)). Complete decorrelation was achieved at approximately 25 cm/s, and normalization was performed for the speckle variance and Doppler variance values relative to full decorrelation.

The flow phantom was then repeated at three different off set locations using a micrometer translation stage (at 220 μm, 355 μm and 465 μm away from zero optical path length delay point) to verify the hypothesis proposed in Section 2. Here, the spot size of the four beams was measured by utilizing a beam profiler and adjust the detector at the same locations with the three off set distances. Figures 5(a)-5(c) show the peak Doppler variance values occurring at the center of the flow channel, averaged across 26400 A-scans, in relation to the mean flow velocity. Figures 5(d)-5(f) show the equivalent peak speckle variance values as the mean flow velocity increased. While varying the imaging depths between these locations, the beam spot size had varied from 13 μm to 77 μm. Despite such a large range of spot size variations, Figs. 5(g)-5(h) showed surprisingly narrow spread of the speckle variance and Doppler variance between the optical beams over the set flow velocity range. To assess the equivalent lateral resolution induced decorrelation change from decreased focal spot beam overlap between A-scans, we plotted the theoretical model of Park *et al.* [37] calculated with the lateral resolution at focus, as shown by the red lines in Figs. 5(g) and 5(h).

3.3 In vivo experiments

3.3.1 Correction of timing-induced phase errors during in vivo experiments

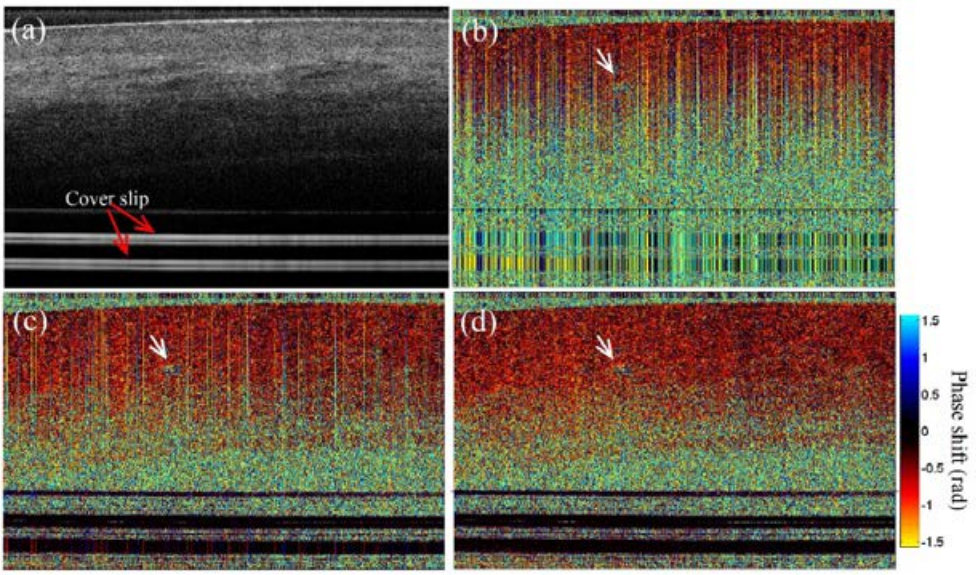

Fig. 6. (a) The structural image of human skin. The cover slip generated a mirrored calibration signal deep to the skin for all 4 beams. (b) Adjacent A-scan derived phase shift image, with timing errors. (c) The phase shift correction as obtained by Vakoc *et al.* [33]. (d) Final corrected phase shift image (without any masking) obtained with the modified method (Eq. (1), showing bulk tissue motion in the background and possible blood flow (arrow).

Human volunteer's skin nail fold imaging was performed to test the feasibility of the above algorithm under *in vivo* conditions. We noted timing-induced system phase errors also

negatively impact our ability in analyzing the enhancement obtained by the new algorithm. We therefore employed a modified phase error correction technique as previously proposed by Vakoc *et al.* [36]. A cover slip was placed between the sample arm scanning head and the zero optical pathlength delay point, such that its mirrored position appear deeper to the skin imaging location to obtain better phase correction effects. The difficulty in applying such technique in a multi-beam arrangement is the possibility of phase wrapping given the different foci depths between the beams. To account for such phase wrappings, let $\Delta\varphi_{i,j}$ and $\Delta\varphi'_{i,j}$ denote the directly measured phase shift and the corrected phase shift, respectively, at depth index i between jth A-scan and (j-1)th A-scan. If the calibration signal is located at depth index L, the phase of calibration signal may be wrapped. To remove phase errors, three phase columns for each A-scan are generated by

$$\Delta\varphi'_{i,j} = \begin{cases} \Delta\varphi_{i,j} - (i/L)\left(\Delta\varphi_{L,j} - \pi\right) \\ \Delta\varphi_{i,j} - (i/L)\Delta\varphi_{L,j} \\ \Delta\varphi_{i,j} - (i/L)\left(\Delta\varphi_{L,j} + \pi\right) \end{cases}. \quad (1)$$

Under normal skin imaging conditions, the standard deviation of the unwrapped phase column is considerably smaller than those of the other two wrapped phase columns. Therefore, we select the phase column with smallest standard deviation as the corrected phase shift. The effect of this calculation is shown in Figs. 6(b)-6(d), where the timing error has been adequately removed to reveal background bulk motion of the subject, and possible microvasculature blood flow (arrow).

3.3.2 Multi-beam 2D color-Doppler OCT imaging

With the timing error corrected phase image, we then proceed to perform multi-beam CDOCT imaging for the human skin. The nailfold on the fourth finger of a healthy volunteer's hand was imaged and the structural images are shown in Fig. 7. Figure 7(a) is a photograph of the finger with the imaging position marked by the black line Figs. 7(b)-7(e) are the images obtained with beam 1 - beam 4, respectively. CDOCT image processing using Kasai autocorrelation with axial window size of 2 pixels and lateral window size of 5 A-lines was performed on these images to extract blood flow information and the results are shown in Fig. 8. Since each beam imaged the same target area with slightly different incident angle with lateral and depth off sets, image alignment was required to allow proper analysis between individual beams. Further, the slight change in incident angle, coupled by sample surface curvature, contributed to individual beam's different imaging plane in the sample which resulted in partial capture of small tortuous microvasculature (as marked by white arrows in Figs. 8(a)-8(d). Such effects would be minimized by 3D imaging (see Section 3.3.4).

Optics EXPRESS

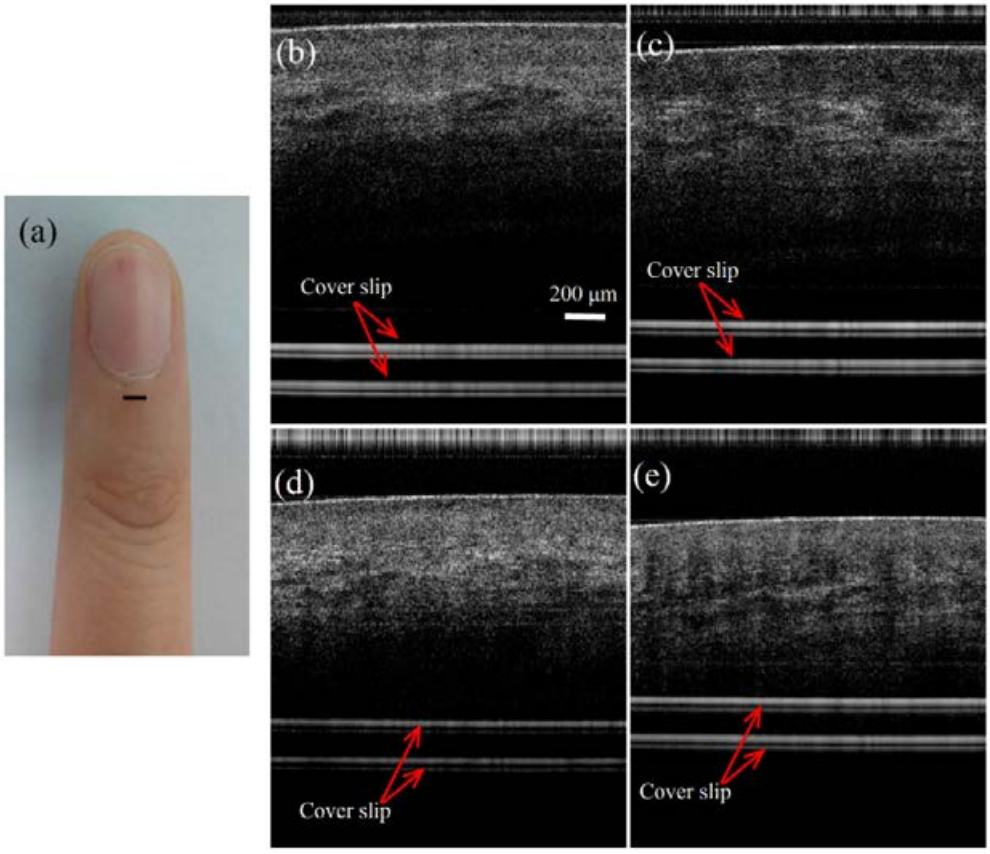

Fig. 7. (a) The photograph of the nailfold on the fourth finger of a healthy volunteer's left hand. (b) - (e) are the structural images obtained with beam 1 - beam 4, respectively, at the position marked by a black line in (a).

To evaluate the SNR improvement by using the multi-beam CDOCT imaging, we measured the maximum value of the blood flow signal (S_b) and the standard deviation adjacent to the blood vessel (δ_{bn}) which represented the phase shift noise floor. The SNR of blood flow signal is calculated by $SNR = 20 \cdot \log\left(S_b / \delta_{bn}\right)$ [8]. The individual beams showed SNR ranging from 20 dB to 25 dB, where the averaged multi-beam result showed SNR of 30 dB, with clear improvement.

Optics EXPRESS

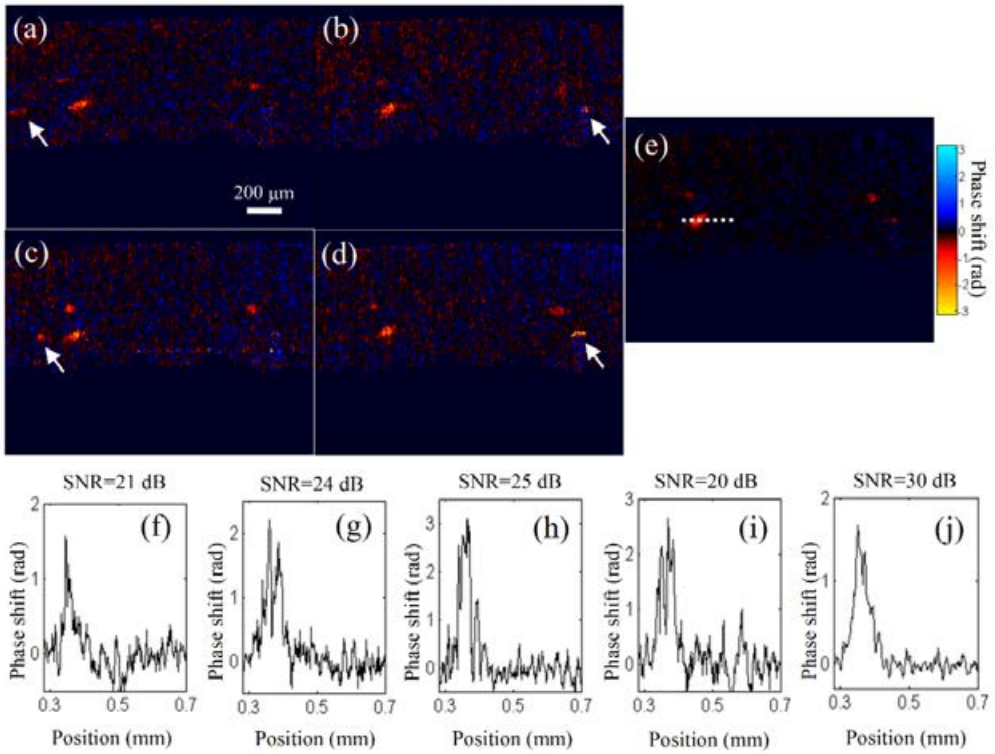

Fig. 8. Multi-beam human nail fold CDOCT, aligned to image the same microvasculature, after structural image intensity thresholding to generate binary mask of phase shift processing. (a) - (d) are the phase shift images obtained with beam 1 - beam 4, respectively. Averaging these 4 images obtained much improved SNR of the phase shift as shown in (e). To quantify the SNR improvement, we plotted depth resolved phase shift along the dotted line for the multi-beam averaged result (j) and all of the individual beams (f) – (i).

3.3.3 Multi-beam 2D Doppler Variance OCT imaging

We then performed DVOCT algorithm on the same raw data with Fig. 7. The results are shown in Fig. 9, with processing window size also set at 2 × 5 pixels. Similarly, we observed SNR improvement by averaging the Doppler variance data from each of the four beams, as the final image Fig. 9(j) showed SNR of 26 dB, which was as much as 11 dB over the individual beam.

Optics EXPRESS

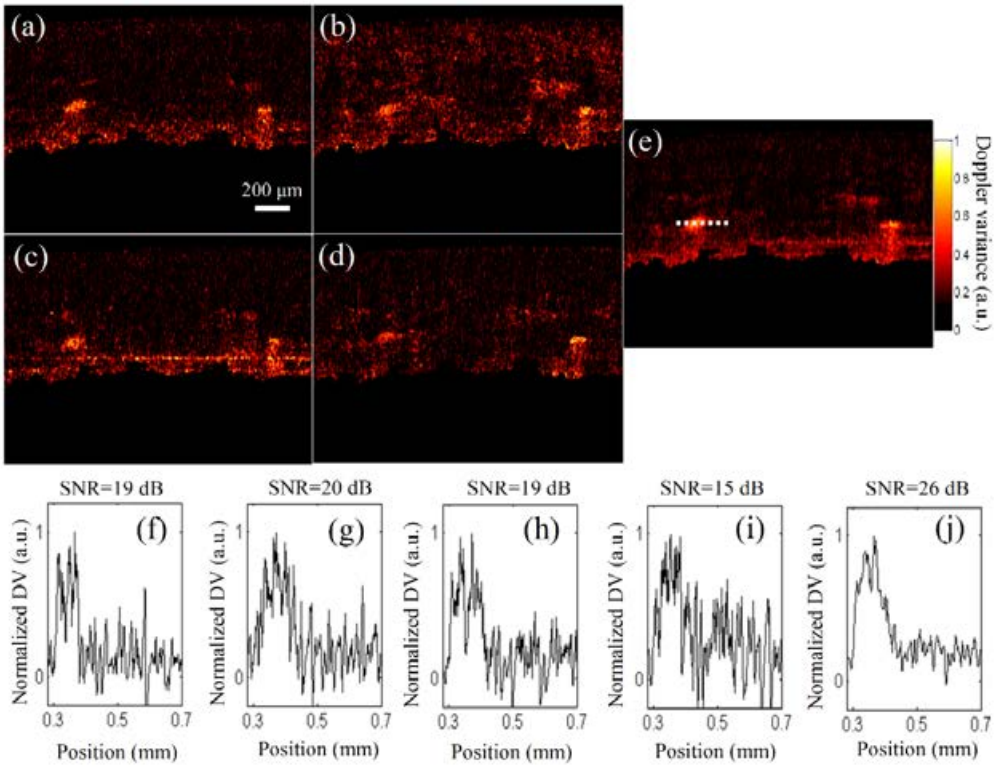

Fig. 9. Multi-beam human nail fold DVOCT, aligned to image the same microvasculature, after structural image intensity thresholding to generate binary mask of Doppler variance processing. (a) - (d) are the Doppler variance images obtained with beam 1 - beam 4, respectively. Averaging these 4 images obtained much improved SNR of the phase shift as shown in (e). To quantify the SNR improvement, we plotted the normalized Doppler variance along the dotted line for the multi-beam averaged result (j) and all of the individual beams (f) – (i).

3.3.4 Multi-beam 2D and 3D speckle variance OCT imaging

3D imaging of the nailfold was then performed over an area of 0.5 mm × 2 mm. Interframe SVOCT processing was performed to extract intensity variance caused by blood flow between adjacent frames. Capillary vessel loops, typically identified in the nailfold, were easily visualized in these 2D and 3D images as shown in Fig. 10. There was clear advantage by combining the SV data from multiple beams, as the final combined SV image showed as much as 10 dB improvements over individual beams. To further quantitative compare the image quality, contrast-noise-ratio (CNR) between vascular signal and background (the regions marked by dashed white rectangle and white rectangle in Fig. 10(o), respectively) was calculated as

$$CNR = \frac{\bar{I}_{dy} - \bar{I}_{bg}}{\sigma_{bg}} \tag{2}$$

where $\bar{I}_{dy}$ and $\bar{I}_{bg}$ are the mean values of the dynamic flow signal and the background, respectively. σ_{bg} is standard deviation of background. The results were shown in Fig. 11 and it can be found CNR can be improved of 23 on average by using the images obtained by all four beams.

Optics EXPRESS

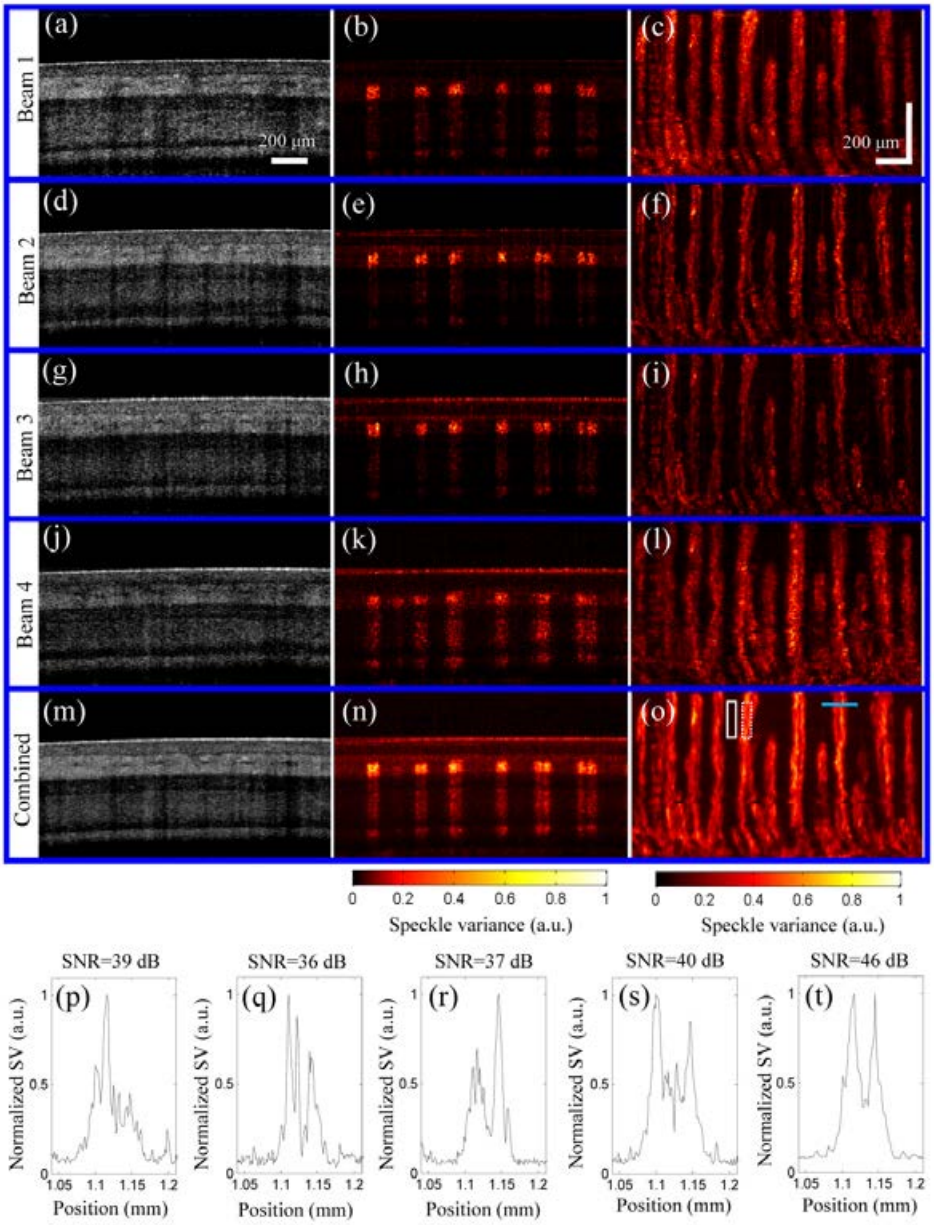

Fig. 10. Multi-beam speckle variance images of the nailfold obtained by interframe SVOCT between adjacent frames. (a) to (o): Each row above showed images from individual beams 1-4 followed by combined multi-beam images. Each column above represented 2D structural, 2D SVOCT, and *en face* maximum intensity projection of the 3D imaging volume. For detailed SV magnitude along the blue line marked in (o), we plotted the normalized speckle variance from beam 1 to 4 in (p) - (s), respectively. The combined multi-beam SVOCT signal (t) achieved a SNR of 46 dB, as much as 10 dB over the individual beams.

Optics EXPRESS

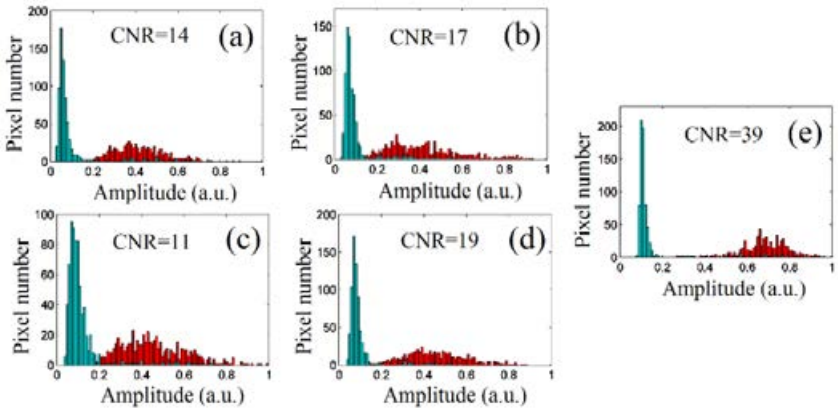

Fig. 11. The speckle variance OCT histogram of background area as marked by solid rectangle in Fig. 10(o) displayed in blue, in comparison to the blood flow area marked by dash rectangle displayed in red. Individual beam results of 1 to 4 are shown in (a) – (d), respectively. (e) The combined result of the images obtained by the four beams, showing improved CNR as the histograms separate.

3.3.5 3D multi-beam SVOCT imaging of a patient's skin lesion with actinic keratosis

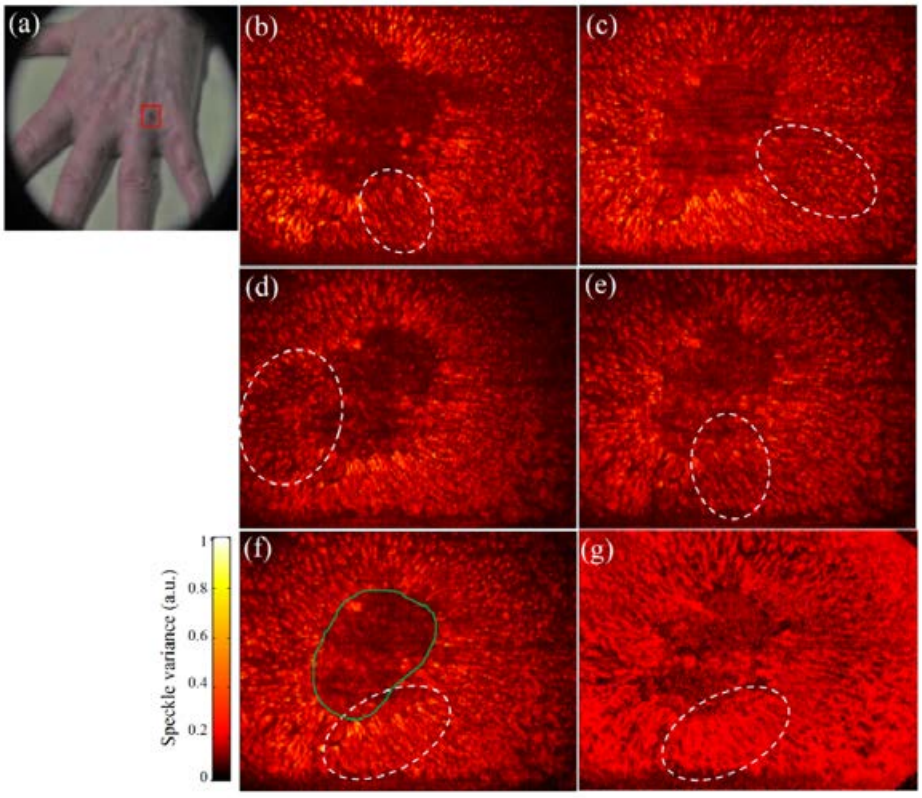

Fig. 12. Multi-beam SVOCT *en face* microvascular imaging of a patient with actinic keratosis on hand. (a) Photograph of the patient's right hand with a skin lesion marked by a red square (6 mm × 6 mm). (b) - (e) are the *en face* microvascular images obtained by the interframe SVOCT method with beam 1 - beam 4, respectively. (f) The averaged *en face* microvascular image, the marked region by green line is the lesion. (g) The *en face* microvascular image exported from the commercial OCT system with lower SNR, where only in-focus data was used.

Optics EXPRESS

In addition to human volunteer imaging, we employed the above multi-beam SVOCT technique in patients with non-melanoma skin cancers (NMSC), as part of a larger clinical study at our institution. Hospital Research Ethics Board approval was obtained for SVOCT imaging in these patients before and after treatment. Among these patients, actinic keratosis was also present, which represented pre-cancerous lesions with potential to develop into NMSC. We present two patients' pre-treatment imaging results here to demonstrate that multi-beam SVOCT can offer higher quality microvascular images. The first patient (Fig. 12) has a small deep lesion on her hand. The whole lesion was scanned and the results show that no blood vessel appears within the lesion area (marked by green line) and a rich fine network of microvasculature surrounding it, providing oxygen and nutrients. The second patient (Fig. 13) has a large superficial lesion on his back, a portion of lesion was scanned and the results show an increased microvascular density within the lesion. In both Fig. 12 and Figs. 13(b)-13(e) are the microvascular images obtained by the interframe SVOCT from the individual optical beams. Comparing these four images, it can be found that the distributions of blood vessels complement each other, as the fine features of the microvasculature are different as marked by the white ellipses. Combining these complementary features resulted in Figs. 12(f) and 13(f), where richer microvascular signals (the regions marked by dashed ellipses) and higher SNR (obviously at the periphery of Fig. 12(f)) were demonstrated compared to the images (Figs. 12(g) and 13(g)) exported from the commercial multi-beam OCT system where only in-focus data was used.

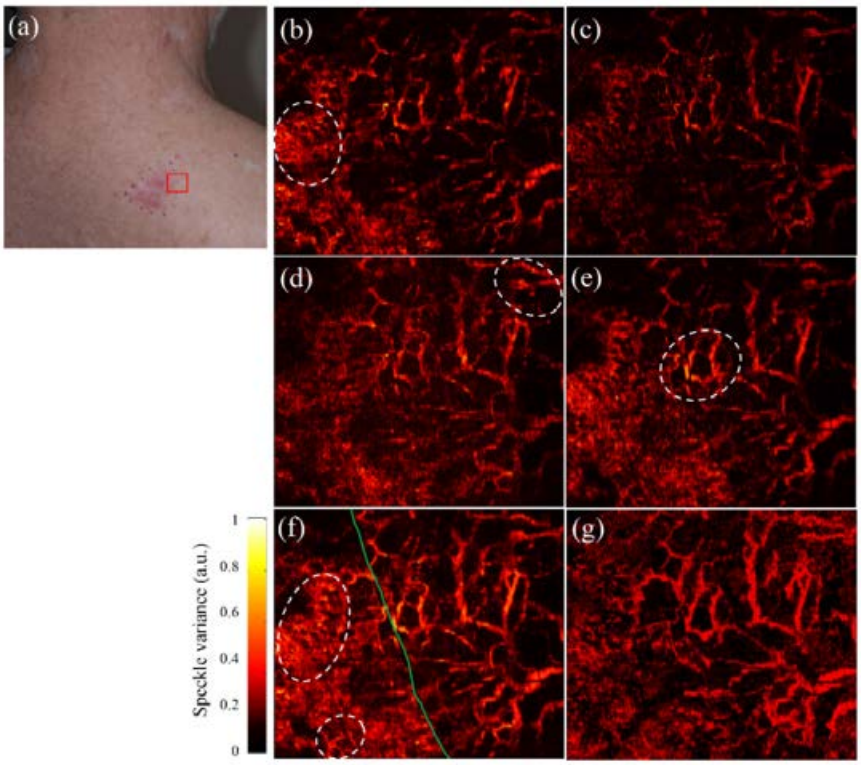

Fig. 13. Multi-beam SVOCT *en face* microvascular imaging of another patient with actinic keratosis on back. (a) Photograph of the lesion and the region marked by a red square (6 mm × 6 mm) was scanned. (b) - (e) are the *en face* microvascular images obtained by the interframe SVOCT method with beam 1 - beam 4, respectively. (f) The averaged *en face* microvascular image, the green line is the boundary of the lesion. (g) The *en face* microvascular image exported from the commercial OCT system, where only in-focus data was used.

Optics EXPRESS

4. Discussion and conclusion

In this paper, we investigated whether multi-beam scanning OCT's staggering optical foci would negatively impact Doppler and speckle based processing techniques in providing microvascular information. In such system's sample arm, four individual optical beams were focused at different depths in a sample, and the resultant structural OCT images were stitched together to obtain improved spatial resolution. Without altering the scanning pattern, the out-of-focus segments of the optical beams still scanned across the target area, and thus still contained valuable information. We initially hypothesized the highly variable focal spot sizes, inherent in the higher numerical aperture associated with multi-beam OCT system, would negatively impact at least some of the blood flow processing techniques, especially the Doppler variance and speckle variance methods. To our surprise, despite the 6 × difference in spot size, the four optical beams showed reasonably similar responses to flow phantom velocity. This formed the basis for combining these data from out-of-focus region, previously discarded, to obtain improved SNR of microvasculature imaging. There was no mechanical scanning penalty. The only requirement was to computationally process these out-of-focus data and average, which proved to be insignificant with current computing hardware typically found on modern OCT systems. The improvement in SNR, however, was significant. In our *in-vivo* human volunteer imaging of the capillary network in the nailfold, we observed as much as 10 dB improvement over individual beam's data. We investigated whether simply averaging the same beam's data four times would reproduce similar results. In Fig. 14, we performed running average of 4 A-scans of the same beam and analyzed the resultant SNR of Doppler shift, Doppler variance, and speckle variance images. In comparison to the combined results from different beams, simply averaging of the same beam only offered 2-3 dB SNR advantage.

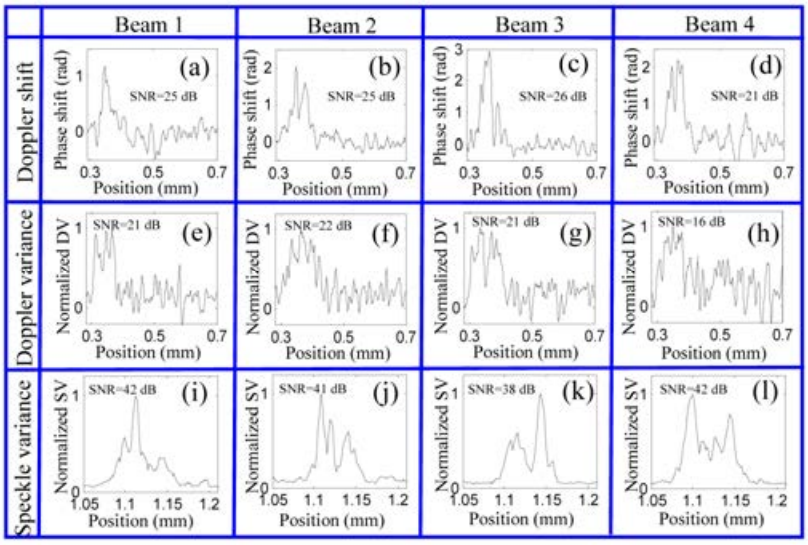

Fig. 14. The SNR comparison after simply averaging 4 A-scan from the same beam. (a) – (d), (e) – (h) and (i) – (l) are the plots from the same data set with those in Fig. 8, Fig. 9 and Fig. 10, respectively.

A further benefit, as demonstrated in the actinic keratosis patient imaging, was likely due to the different Doppler angles of each individual optical beam interrogating the same microvasculature. The four optical beams often produced similar yet subtly different blood flow maps. Combining them together, effectively providing angular compounding, resulted in higher quality lesional microvascular maps.

We noted the key limitation of our technique was closely linked to its advantage, since this technique required out-of-focus data which were only available to staggered multi-beam OCT systems. In addition, depending on the sample arm optical design, there could be small but non-zero Doppler angle differences between each beam, causing systematic error in the Doppler shift measurement. This latter limitation would be incompletely correctable by system calibration, since the surface curvature variation on biological samples would not be fully predictable.

Multi-beam OCT imaging had previously demonstrated its advantage in providing higher numerical aperture, more uniform spatial resolution throughout imaging depth, and improved structural OCT image quality. To our knowledge, this is the first report of effectively utilize previously discarded out-of-focus multi-beam OCT data to synergistically generate optimized Doppler and speckle variance images, without mechanical scanning penalty, and achieve significant SNR improvements.

Acknowledgments

This work was supported by the Graduate School of Nanjing University of Science and Technology, the Michelson Diagnostics, the Canadian Institutes of Health Research, the Natural Sciences and Engineering Research Council of Canada, the Ontario Brain Institute, Ryerson University, the Canada Research Chair Program, the Canada Foundation for Innovation, and the National Natural Science Foundation of China (61275198).